IEEE Access
Multidisciplinary | Rapid Review | Open Access Journal

Received November 19, 2018, accepted December 7, 2018, date of publication December 13, 2018,
date of current version January 7, 2019.

Digital Object Identifier 10.1109/ACCESS.2018.2886563

Scene-Awareness Based Single Image Dehazing Technique via Automatic Estimation of Sky Area

HUI FU, BIN WU, YANHUA SHAO, AND HONGYING ZHANG
School of Information Engineering, Southwest University of Science and Technology, Mianyang 621000, China

Corresponding author: Hui Fu (1285110730@qq.com)

This work is supported by the National Natural Science Foundation of China Fund 61601382, in part by the Scientific Research Fund of SiChuan Provincial Education Department 17ZB0454, and in part by the Fund of Robot Technology Used for Special Environment Key Laboratory of Sichuan Province under Grant 15kftk05, Funded by Longshan academic talent research supporting program of SWUST (17LZX682, 18LZX632).

ABSTRACT The occurrence of fog, mist, smog, or haze significantly reduces the visibility of the scenes and images, resulting in limited recognition of computer vision and computer graphics. So, removing haze from images is a must. In this paper, we regard image dehazing as a mathematical inversion process and image restoration based on atmospheric scattering models. The atmospheric light can be accurately estimated by combining the gray threshold segmentation and the skyline method. The improved least squares filtering method is used to optimize the transmittance map so that the edge details can be highlighted and the halo effect can be alleviated. A large number of test images show that our algorithm can achieve better experimental results than the other seven most advanced dehazing strategies.

INDEX TERMS Grey-level threshold segmentation, skyline, least-square filter, halo artifact, dehazing.

I. INTRODUCTION

In digital image processing, ensuring accurate image extraction is the key. In haze or fog conditions, the details of objects in the image are often unclear due to the suspended particles in the atmosphere. Nevertheless, current computer vision systems are increasingly relying on clear and high quality images. Therefore, how to deal with the visual effects of the images caused by bad weather is extremely important. Moreover, even in good weather conditions, due to the suspended dust in the air and water vapor, and the limitations of the hardware, the images obtained by the processor are often poor in quality, which largely increases the risk of algorithm failure in continuous image processing. To update the hardware devices requires funding. Therefore, it is not quite possible. In this backdrop, it is more realistic to improve the dehazing quality and image processing algorithms to cope with the haze problems in the pictures. Our research has wide applications in the computer-based vision systems, such as security surveillance, machine learning, feature recognition, object detection etc., as well as many scene-based applications such as driving assistance, navigation, traffic monitoring, target recognition, crime investigation, routine monitoring in industrial areas, astronomical observation, etc.

In recent years, great achievements have been made in the field of dehazing. Dehazing techniques can be briefly divided into two types: image enhancement-based techniques and image restoration-based techniques. Image enhancement-based techniques include histogram equalization algorithms [1], [2], retinex algorithm [3], [4], homeostasis filtering [5], wavelet transformation [6], and so on. By using the histogram equalization algorithm to extend the dynamic range, the overall contrast of the foggy image can be roughly enhanced [1], but the same processing is applied to all pixels, inevitably losing detail and gray levels. Raffei *et al.* [2] used the local histogram equalization method to divide the image into sub-blocks that do not overlap, but this method takes a lot of time and cannot obtain the optimal value of each local region. In Jiang's method [3], the balance of colour constancy and dynamic range control can be effectively maintained. However, due to the poor edge retention of this method, the halo effect and colour shift phenomenon always appear near the obvious area of edge mutation. In Seow's method [5], in order to improve image quality, he combined a spectral shaping and gradation transformation algorithm. This method can effectively maintain the contour information of the uneven area, but may fail if the calculation amount of the item is large. By combining the restoration of the low frequency region and the enhancement of the high frequency region, in the algorithm [6], the wavelet transform can significantly improve the image quality [6].

Tan [7] found that the contrast of the fog-free image is higher than that of the haze image. This method achieves a better effect by increasing the contrast of the foggy image as much as possible. However, since the contrast of the real scene can hardly be recovered, the processing result of the Tan method is often supersaturated and unnatural. Zhang *et al.* [8] proposed a visibility enhanced dehazing algorithm based on polarization imaging. However, excessive illumination and unevenness may occur in dehazing results. In short, due to the need for visual perception and ease of computer recognition, physical models (inherent properties of image degradation) that tend to degrade images are often not considered in enhancement-based techniques.

To solve the ill-conditioning puzzle, restoration methods based on extra priors conditions or constraints have been proposed. Fattal [9] assumed that the transmittance medium is not correlated with the surface shading of the scene, so the transmittance can be roughly estimated using the scene albedo. However, this method has its limitations on the dehazing process in the absence of statistical information. Mutimbu and Robles-Kelly [10] restored the haze image with the Markov random field, where the scene albedo and the scene depth are two separate statistics. In this approach, the fine edge detail of the fog-free image can be recovered by restoring the decomposition of the typical desired maximum, but the output image is over-enhanced. In order to obtain the exact value of atmospheric light A, Berman *et al.* [11] used a fast bilateral filtering method to optimize the dehazing method. However, the processing speed of the Berman algorithm is slower than the Tarrel algorithm using the median filter [12]. He *et al.* [13] proposed the well-known hypothesis of dark channel prior (DPC) and estimated the transmittance based on a large number of observations. The intensity of a DPC, i.e., a fog-free pixel, typically includes at least one RGB colour channel being zero or near zero. DCP technology can achieve impressive dehazing effects, but it does not correctly handle image areas where the brightness is substantially similar to dynamic atmospheric light values. At present, various DCP-based algorithms [14]–[16] have been proposed. However, with the processing algorithm based on the DCP model, the transmittance map is not smooth and there is image noise also. He *et al.* [17] used a soft matting algorithm to suppress block and halo effects. However, the soft mapping algorithm takes up most of the processing time. Therefore, He *et al.* [18] further used an effect-improving edge-preserving algorithm-steering filter to optimize the transmittance, thereby reducing the computational cost.

By studying both the image enhancement dehazing and restoration-based dehazing algorithms inside China and of the world, we find three problems in the existent studies: (1) The enhancement dehazing method is unable to avoid color distortion and/or color shift for it only relies on increasing the color contrast and the brightness of haze images. (2) Inaccurate estimation of atmospheric light A and transmittance will lead to gradient inversion effects, large image noise, and low efficiency. (3) For haze images with a large proportion of sky area or water space, it may cause over-exposure and mirror reflection and may create a distorted foreground color.

To solve the above-mentioned problems, we propose a novel dehazing method based on precise estimation of the atmospheric light A and transmittance. Our experiments show that the Gray-level threshold segmentation algorithm [19] can not only locate a specific target position but is very efficient. The modified least-square filter method can help retain the details of the images and suppress noise as well, hence offering a good visual sensory experience.

Therefore, in this paper, the Gray-level threshold segmentation algorithm, which is suitable to large areas of sky and water, is used to locate the approximate area of the atmospheric light A, and the skyline method is used to accurately identify the A value. Besides, a modified least-square filter is employed to optimize the transmittance. The experiments results show that our dehazing results not only perform better in image quality, but also are closer to the natural state of the images.

II. RELATED WORK

A. THE ATMOSPHERIC SCATTERING MODEL

The Atmospheric Scattering Model [20], [21] has been widely used in the field of machine vision and computer graphics, and its formula is as follow:

$$F(x, y) = R(x, y)t(x, y) + A(1 - t(x, y)) \tag{1}$$

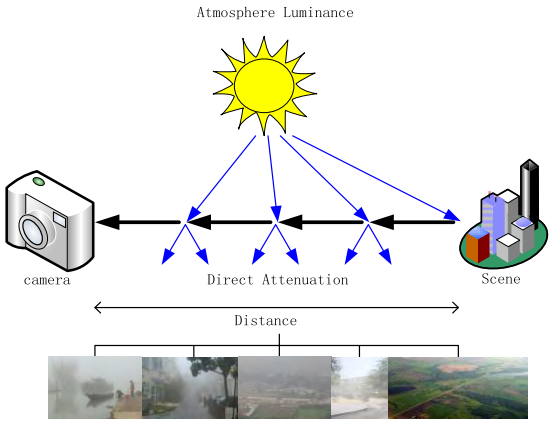

FIGURE 1. The atmospheric scattering model.

In this formula, $F(x, y)$ represents the pixel value of the haze image at the point (x, y), and $R(x, y)$ the pixel value of the haze-free image at the point (x, y) and $t(x, y)$ the transmittance. A is the atmospheric light value and is usually considered to be the maximum intensity of the sky region.

As the atmospheric scattering model is given, the aim of the paper is to estimate A and $t(x, y)$ with only the known parameter $F(x, y)$. Restoring blurred images with limited information is a challenge due to the ill conditioning nature of atmospheric scattering models.

We assume that the pictures were taken in an atmospheric environment with the same homogeneous medium, and the transmittance $t(x, y)$ can be expressed as:

$$t(x, y) = e^{-\beta d(x,y)} \tag{2}$$

β refers to the scattering coefficient of atmospheric light, $d(x, y)$ the depth field. The exponential attenuation relationship between the received light intensity and the depth of field obtained in scenes can be shown in this formula.

From the perspective of computer graphics, the equation of the atmospheric scattering model indicates that the atmospheric light A holds the geometric correlation with $F(x, y)$ and $R(x, y)$, and the transmittance $t(x, y)$ can be represented by the ratio of two line segments.

$$t(x, y) = \frac{||A - F(x, y)||}{||A - R(x, y)||} = \frac{A^C - F(x, y)}{A^C - R(x, y)} \tag{3}$$

B. DARK-CHANNEL

In non-sky areas, based on the definition of DCP, there exists at least one colour channel with quite low pixel value, or even close to 0. The dark channel value of resultant haze-free image $R(x, y)$, obtained in the atmospheric scattering model, can be described by Eq.(4).

$$R^{\text{dark}}(x, y) = \min_{z \in \Omega(x,y)} \left(\min_{C \in (r,g,b)} R^C(z) \right) = 0 \tag{4}$$

Here, C denotes the RGB colour channel of pixel (x, y) in haze-free image $R(x, y)$, Ω (x, y) the pixel block around (x, y). There are three main reasons for low pixel values in dark channels: shadows, colored targets, and dark targets.

C. DARK-CHANNEL PRIOR ALGORITHM

We suppose that the atmospheric light A^C has been given, then Eq.(1) can be transformed to Eq.(5) by A^C.

$$\frac{F^C(x, y)}{A^C} = t(x, y)\frac{R^C(x, y)}{A^C} + 1 - t(x, y) \tag{5}$$

Based on the fact that every colour channel is independent, we make dark-channel calculation to the both sides of the equation by assuming that transmittance will remain constant at Ω(x, y).

$$\min_{Z \in \Omega(x,y)} \left(\min_{C \in [r,g,b]} \left(\frac{F^C(x, y)}{A^C} \right) \right) = t(x, y) \min_{Z \in \Omega(x,y)} \left(\min_{C \in [r,g,b]} \left(\frac{R^C(x, y)}{A^C} \right) \right) + 1 - t(x, y) \tag{6}$$

Then one term can be eliminated and t (x, y) can be got by substituting Eq.(4) into Eq.(6), as shown in Eq.(7).

$$t(x, y) = 1 - \min_{Z \in \Omega(x,y)} \left(\min_{C \in [r,g,b]} \left(\frac{F^C(x, y)}{A^C} \right) \right) \tag{7}$$

The resultant images will be quite unnatural if haze is entirely eliminated. So we retain a certain amount of fog for the distant target object, and introduce parameter w_0 into Eq.(8) for adjustment. Based on the validity of multiple experiments, the value of w_0 is usually set to 0.95.

$$t(x, y) = 1 - w_0 \min_{Z \in \Omega(x,y)} \left(\min_{C \in [r,g,b]} \left(\frac{F^C(x, y)}{A^C} \right) \right) \quad 0 < w_0 < 1 \tag{8}$$

In He's method [18], the value of λ can be set as 10^{-4}. Considering U and L are unit Laplacian matrices with the same size, calculation of soft matting algorithm is adopted to obtain the optimized transmittance t_1(x, y).

$$(L + \lambda U)t(x, y) = \lambda t_1(x, y) \tag{9}$$

III. PROPOSED STRATEGY

In many restoration-based techniques, strong visual effect areas in haze images can inevitably be selected to estimate atmospheric light A, which leads to reflection problems. For example, the surface of the reflector is often used incorrectly for the estimation of A. In He's method [18], it is confirmed that the atmospheric light A is set by selecting the first pixel maximum pixel value in the entire image, which results in low A precision. In the paper, Gray-level threshold segmentation algorithm [19] is employed to separate and locate the approximate region of atmospheric light value A, and then the maximum value of atmospheric light is identified by the skyline method. Hence, the atmospheric light A is obtained accurately. Besides, the efficiency of our algorithm can be improved by estimating transmittance through modified least-square filter.

A. GRAY-LEVEL THRESHOLD SEGMENTATION

The purpose of adopting Gray-level threshold segmentation algorithm [19] is to separate the approximate area S, which involve the atmospheric light A from the background. It is crucial to select the appropriate threshold value in Gray-level threshold segmentation algorithm. Based on the prior information, we can learn that most of the atmospheric light has pixel values between 218 and 223. So in this paper, the threshold value can be manually set to 215 in order to save the processing time. By setting a single threshold value, Gray-level threshold segmentation algorithm can effectively divide initial haze images into the background and the target. In this section, firstly, the original image is transformed into a Gray-level image, then the probability of every gray level is used to draw a histogram.

Here, $F_1(x, y)$ denotes the segmented image of $F(x, y)$, T the selected threshold value and is set to 215 on the basis of the experiments. The basic formula is as follows:

$$F_1(x, y) = \begin{cases} 0 & F(x, y) < T \\ 1 & F(x, y) > T \end{cases} \tag{10}$$

B. IN SEARCH OF LIGHT A BY USING SKYLINE ALGORITHM

As described above, the approximate area S which contains the atmospheric light A is obtained by Gray-level threshold

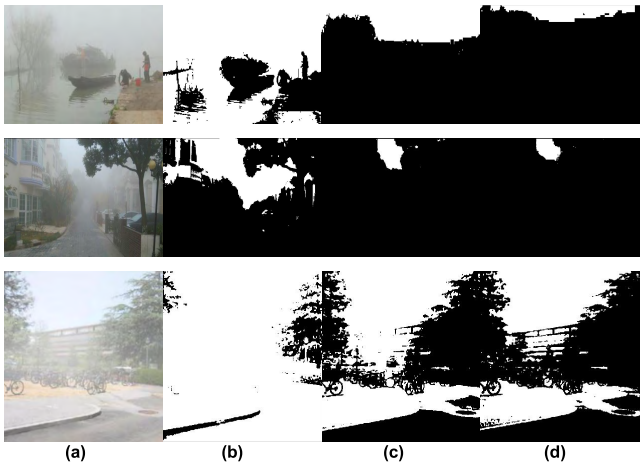

FIGURE 2. Approximate region of *A* positioning using Gray-level threshold segmentation algorithm with different *T*. (a) Original picture. (b) *T*=150. (c) *T*=200. (d) *T*=215.

segmentation. In order to accurately acquire atmospheric light A, we use skyline algorithm to search in area S. The function of skyline algorithm [22] is to make the optimum choice. In other words, this is a way to find the maximum pixel value in the area S, and use that value as A.

The searching strategy of skyline algorithm is to find the control points. Assuming there are two points $E[i] = [E[1], E[2], ..., E[n]](i\epsilon[1, n])$ and $F[i] = (F[1], F[2], ..., F[n])$. To satisfy the condition that the value of $E[i]$ is not worse than $F[i]$ in any dimension, and $E[i]$ must be stronger than $F[i]$ in at least one dimension, then we can express that $E[i]$ control $F[i]$. In brief, if $E[i]$ and $F[i]$ satisfy $E[i] \geq F[i]$, and $E[i] > F[i]$ in at least one dimension, then the point $E[i]$ controls another point $F[i]$.

Supposing there are points $E[i]$, $F[i]$, $G[i]$, $H[i]$, $I[i]$, $J[i]$, $K[i]$ in two-dimensional coordinate system, which we can see clearly in Fig.3. $F[i]$, $H[i]$ and $I[i]$ are controlled by $E[i]$, $H[i]$ and $I[i]$ are controlled by $G[i]$, $K[i]$ is controlled by $J[i]$. While $E[i]$, $G[i]$ and $J[i]$ are not controlled by any point, so these points are skyline points. By comparing the skyline points, the maximum value can be set to atmospheric light A.

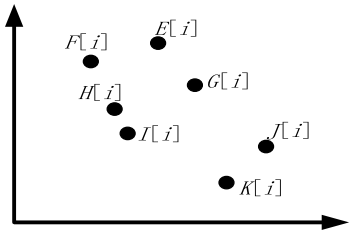

FIGURE 3. Skyline model.

C. MODIFIED LEAST-SQUARE FILTER METHOD TO OPTIMIZE TRANSMITTANCE

In the process of dehazing, the use of the original transmittance leads to the problem of deep discontinuity. For the original transmittance, He *et al.* [13] used soft matting algorithm to process the transmittance, which is costly and time consuming. Considering that the transmittance $t(x, y)$ and depth of field are in exponential relationship as shown in Eq.(2), large deviations on field of depth along the edges can hardly be avoided. Besides, there are often serious halo effects in edge areas of the haze images. The selected algorithms should preserve as many edge details as possible while removing noises. The least-square filter method [23] is widely used in image restoration, and has performed well in maintaining image details, However, it is susceptible to image noises. In this paper, the modified least-square filter is used to optimize the transmittance. It can also avoid the defects of traditional least-square filter. The modified least-square filter [24] can not only preserves the fringe details of the projected image but also minimizes noise to the largest extent.

The mathematical expression of the least-square filter is based on the two-dimensional discrete convolution of image degradation model, and it can be modified by introducing constraints. In the image degradation model, $f(x, y)$ is the original image, $n(x, y)$ the correlated noise, and $g(x, y)$ the degraded image.

$$g(x, y) = H[f(x, y)] + n(x, y) \tag{11}$$

The discrete model of two-dimensional convolution is as follows:

$$h(x, y) * f(x, y) = \frac{1}{MN} \sum_{m=0}^{M-1} \sum_{n=0}^{N-1} f(m, n)h(x - m, y - n) \tag{12}$$

For the linear operators B_1 and B_2, provided in modified least-square filter [24], the optimized transmittance $t_1(x, y)$ is structured as $||B_1 t(x,y)||^2 + ||B_2 t(x,y)||^2$, and satisfies the condition of $||t(x, y) - Ht_1(x,y)||^2 = ||n(x, y)||^2$. In order to calculate the minimum value, the Lagrange factor λ should be selected on the basis of the two conditions above. We can structure the function as follows.

$$\begin{aligned} J(t_1(x, y)) = &||B_1 t(x, y)||^2 + ||B_2 t(x, y)||^2 \\ &+ \lambda(||t(x, y) - Ht_1(x, y)||^2 - ||n(x, y)||^2) \end{aligned} \tag{13}$$

The differential operator is used to obtain Eq.(14).

Assuming that $R_{t(x,y)}$ and $R_{n(x,y)}$ are the auto-correlation matrices of t (x, y) and n (x, y), respectively, and we define $B_1^T B_1 = R_{t(x,y)}^{-1} R_{n(x,y)}$, $B_2^T B_2 = C^T C$.

$$\begin{aligned} \frac{\partial J(t_1(x, y))}{\partial(t_1(x, y))} = &2B_1^T B_1 t(x, y) + 2B_2^T B_2 t(x, y) \\ &+ (2\lambda - 2\lambda H^{-T})t(x, y) = 0 \end{aligned} \tag{14}$$

$$t_1(x, y) = (1 + \frac{1}{\lambda} B_1^T B_1 + \frac{1}{\lambda} B_2^T B_2 - H^{-T})^{-1} t(x, y) \tag{15}$$

$$\begin{aligned} t_1(x, y) = &(1 + \frac{1}{\lambda} R_{t(x,y)}^{-1} R_{n(x,y)} + \frac{1}{\lambda} C^T C - H^{-T})^{-1} \\ &\times t(x, y) \end{aligned} \tag{16}$$

We set the diagonal matrix as D, A, B, E, and define $H = WDW^{-1}$, $R_{t(x,y)} = WAW^{-1}$, $R_{n(x,y)} = WBW^{-1}$,

$C = WEW^{-1}$, then formula (16) is converted to formula (17).

$$t_1(x, y) = (1 + \frac{1}{\lambda} WABW^{-1} + \frac{1}{\lambda} WE^*EW^{-1} - WD^{*-1}W^{-1})^{-1} t(x, y) \quad (17)$$

The improved transmittance $t_1(x, y)$ is transformed to a frequency domain expression by convolution model, as shown in Eq.(18) :

$$T_1(u, v) = [\frac{H^*(u, v)}{|H(u, v)|^2 + \frac{1}{\lambda}[S_n(u, v)/S_t(u, v) + \frac{1}{\lambda}[p(u, v)]^2]}] \times T(u, v) \quad (18)$$

In it, $H(u, v)$ and $T(u, v)$ are the Fourier conversions of the point spread function (PSF) $h(x, y)$ [25] and the initial transmittance $t(x, y)$, respectively. $S_t(u, v)$ means the power spectrum [26] of the initial transmittance, $S_n(u, v)$ the noise power spectrum, $T_1(u, v)$ and $p(u, v)$ the Fourier conversion of optimized transmittance and Laplace operator [27], respectively. Fig.4 presents the initial images, gray-scale images, the transmittance after the guided filtering by He's method, and the transmittance of our method herein. Compared with He's approach [18], the transmittance of our method can obtain more overall information and its edge parts are closer to the natural state.

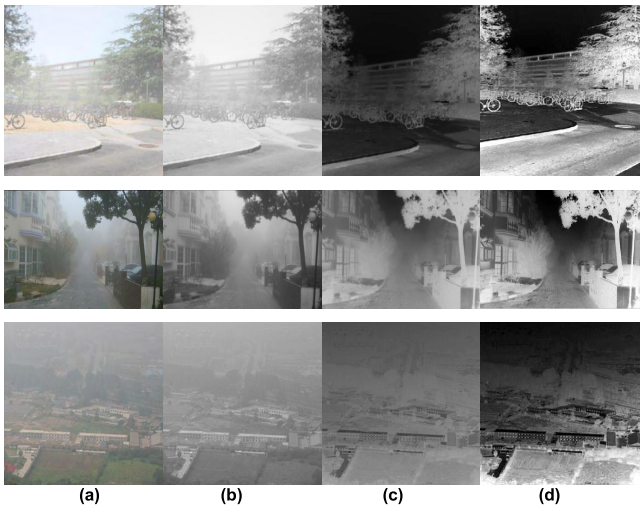

FIGURE 4. Comparison of transmittance processed by guide filter and modified least-square filter. (a) Haze images. (b)Original transmittance. (c) Transmittance processed by guide filter. (d) Transmittance processed by modified least-square filter.

For the foggy images of "road", "community", and "city", Fig.5 shows the three-dimensional (3D) representation of the transmittance after being processed by the algorithms [10], [11], [16], [18] and our method. It can be clearly seen that the halo effects in the red box are moderated by our method. However, the individual pixels of algorithms [10], [18] in the red box area are protruded due to noise. The improved algorithm [16] based on algorithm [18] can not avoid the deficiency mentioned above. As we can see, in our algorithm, the dynamic range and image contrast

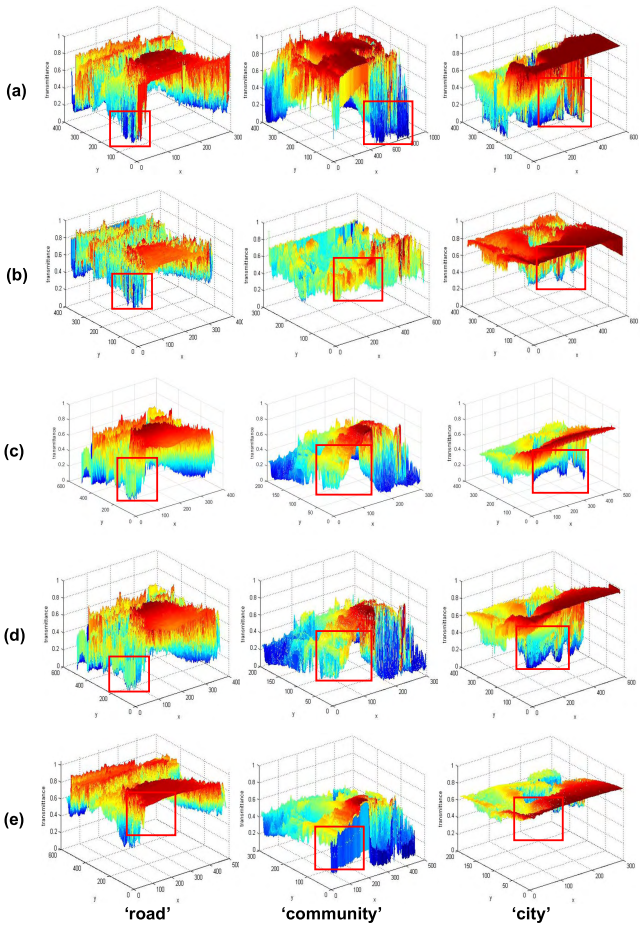

FIGURE 5. Transmittance of restoration-based techniques. (a) The algorithm [10]. (b) The algorithm [11]. (c) The algorithm [16]. (d) The algorithm [18]. (e) Improved algorithm.

can be expanded and boosted without enlarging the noise. In Fig.5, we can see that the transmittance processed by technique [11] and our technique are smoother than algorithms [10], [16], [18]. This is because the transmittance of our method retains the maximum amount of information in the four methods while the transmittance of the algorithm [11] contains plenty of details.

Besides, the transmittance performance of our algorithm and other four restoration-based algorithms are also related to the average SSIM [28], [32] index values of R, G and B colour channel. As can be seen from Table 1, our method obtained a better transmittance.

TABLE 1. The indexes of SSIM [28], [32] for R, G, B.

SSIM	R	G	B
Method [3]	0.8192	0.7533	0.6782
Method [10]	0.9102	0.7328	0.6215
Method [11]	0.9325	0.7536	0.6328
Method [16]	0.8655	0.8023	0.6531
Method [18]	0.8537	0.7903	0.6725
Improved method	0.9661	0.8826	0.7215

D. IMAGE DE-HAZING

As the atmospheric light A and the transmittance are obtained, on the basis of Eq.(1), the haze-free image scene $R(x, y)$ can be given by Eq.(19).

$$R^C(x, y) = \frac{F^C(x, y) - A^C}{\max\{t_1(x, y), t_0\}} + A^C \tag{19}$$

Here, t_0 is the low limit of the transmittance and can be set to 0.1 based on the empiric value. Fig.6 shows the procedure of our method.

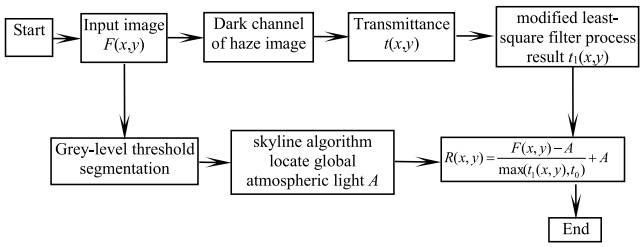

FIGURE 6. Improved algorithm flowchart.

IV. EXPERIMENT AND RESULT

In order to verify the reliability of our method, the effect of our method is compared with that of the other seven state-of-the-art methods. The experiments run on a computer with Inter corei7-990X 5GHz CPU and 4GB memory. MATLAB 2017a is operated on Windows 8 system. The test set used in this paper are either downloaded from the Internet or taken by us. Altogether 418 real-world fog scenes and 100 synthetic fog scenes of lake views, architectures, fields, woods, suburban landscapes, street corners, bird-view landscapes, vistas and close-ups etc. are used in our experiments [33].

A. VISUAL ASSESSMENT

We choose five kinds of fog-day images from the test set to conduct the comparison experiments. Five groups of haze removal results are presented in following illustrations, which are named as 'boat' (resolution ratio: 280∗320), 'community' (resolution ratio: 350∗550), 'city' (resolution ratio: 400∗600), 'road' (resolution ratio: 500∗800), 'field' (resolution ratio: 960∗1280). In Fig.7, Fig.8, Fig.9, Fig.10, and Fig.11, (a) is the original image, (b)-(i) are the dehazing results.

The large scale of sky and lake areas in Fig. 7 (a) occupies the entire image, which presents a challenge to the haze removal process and is prone to specular reflection problems [29] if improperly handled. The visual effects of Fig. 7 (b)-(i) are enhanced after being processed by using our approach and seven other advanced algorithms. In Fig.7 (b) and Fig.7 (c), the algorithms [3], [4] significantly improve the contrast of the output image. However, most of the dehazing image areas have the colour shift phenomenon. The contrast and definition of Fig.7 (d) are significantly enhanced, while unnatural color depth and block effects occur in areas with significant depth changes. Fig.7 (e) has good visual

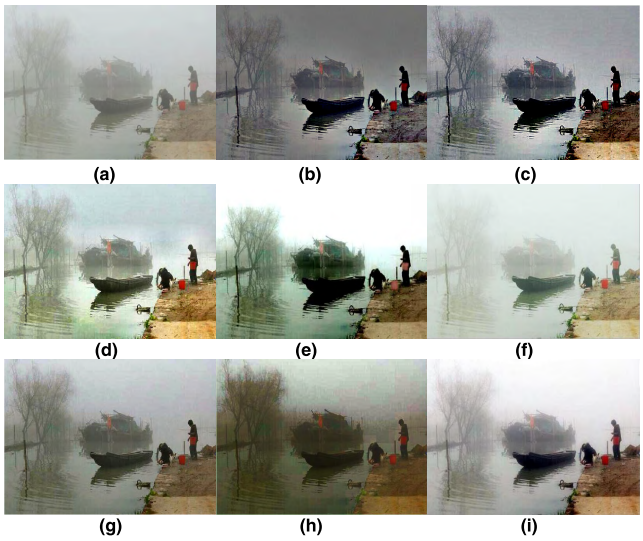

FIGURE 7. Comparison of different dehazing algorithms. (a) Haze image (b) The algorithm [3]. (c) The algorithm [4]. (d) The algorithm [8]. (e) The algorithm [10]. (f) The algorithm [11]. (g) The algorithm [16]. (h) The algorithm [18]. (i) Improved algorithm.

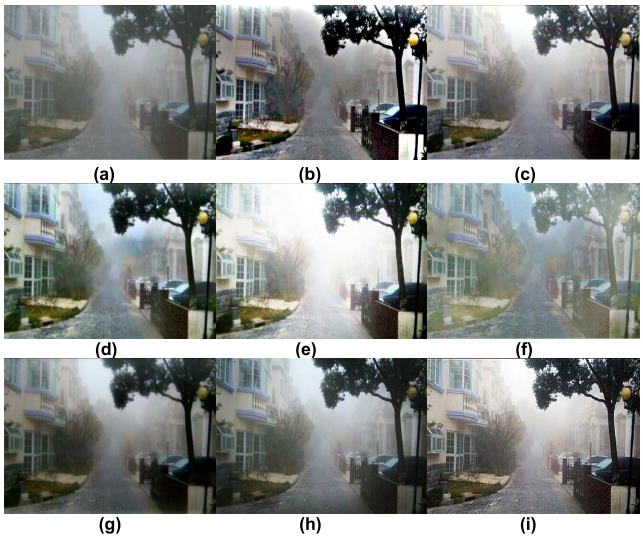

FIGURE 8. Comparison of different dehazing algorithms. (a) Haze image (b) The algorithm [3]. (c) The algorithm [4]. (d) The algorithm [8]. (e) The algorithm [10]. (f) The algorithm [11]. (g) The algorithm [16]. (h) The algorithm [18]. (i) Improved algorithm.

effects, but the foreground colour in Fig. 7(e) is unnatural. Method [10] demonstrates the problem of oversaturation, hence causes the look of pure white sky area in Fig.7(e). We note that the result image from Fig.7(f) is blurred by the edge details, which means that the estimation of the atmospheric light A is inaccurate. Besides, similar inaccurate estimation problem result in dark luminance of Fig.7 (g) and Fig.7(h). As shown in Figure 7 (i), the de-fogging effect of our method is more natural.

As regard to the dense haze image shown in Fig.8 (a), the visual quality is greatly improved by algorithms [3], [4], [8], [10], [11], [16], [18] and our algorithm, and

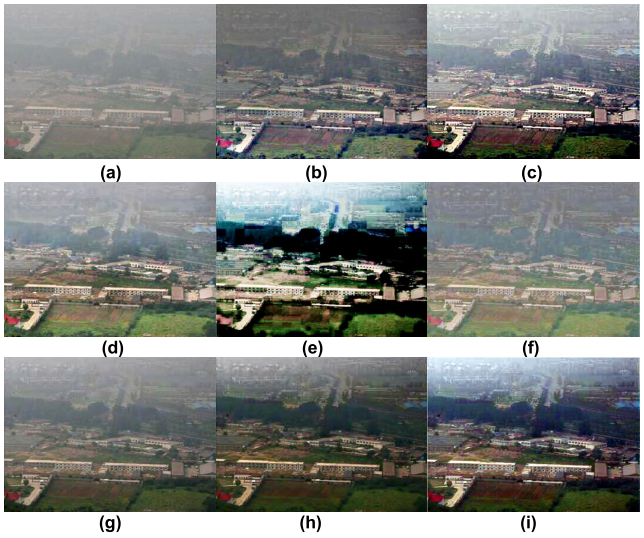

FIGURE 9. Comparison of different dehazing algorithms. (a) Haze image (b) The algorithm [3]. (c) The algorithm [4]. (d) The algorithm [8]. (e) The algorithm [10]. (f) The algorithm [11]. (g) The algorithm [16]. (h) The algorithm [18]. (i) Improved algorithm.

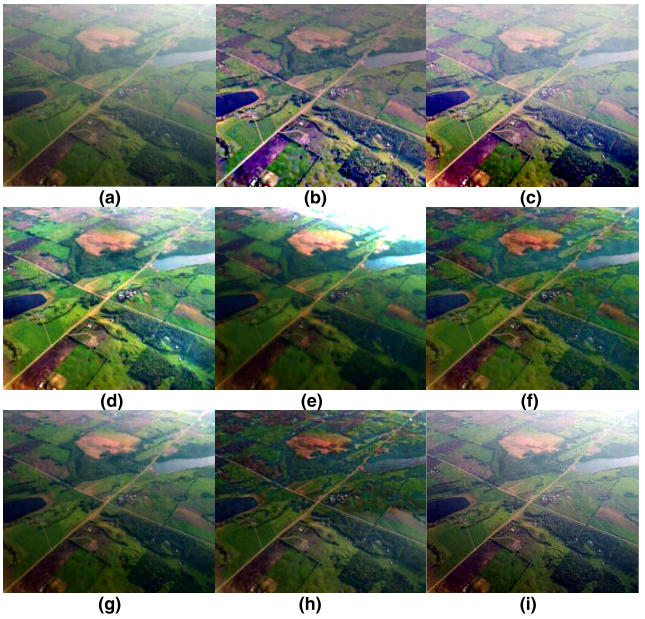

FIGURE 10. Comparison of different dehazing algorithms. (a) Haze image (b) The algorithm [3]. (c) The algorithm [4]. (d) The algorithm [8]. (e) The algorithm [10]. (f) The algorithm [11]. (g) The algorithm [16]. (h) The algorithm [18]. (i) Improved algorithm.

the above mentioned algorithms can alleviate the effect of haze to some extent. Among those, algorithms [4], [16], [18] and our algorithm can obtain better visual effects in dense haze images when the depth of scene changes rapidly. This is because that the transmittance acquired by algorithms [16], [18] and our algorithm are more close to the natural state; the visual effect is primarily considered in algorithm [4]. For Fig.8(d) and Fig.8(f), we used the algorithms [8], [11], which demonstrate colour shift phenomenon and image noise.

Fig.9 presents a downward landscape, however, directed at the border of buildings and trees in dehazing images, there are colour cast phenomenon in techniques [3], [10], as we can see in Fig.9 (b) and Fig.9 (e). By artificially enhancing the image contrast, Fig.9 (c) has bright image foreground color. The haze-free images tend to yield colour shift in different degrees, as shown in Fig.9(d) and Fig.9(f). Techniques [16], [18] behave better in keeping close to the colour of the source image, yet it is lack of competitiveness in overall effect, and the details are shown in Fig.9(g) and Fig.9(h). Fig.9(i) shows the haze removal results handled by our algorithm. As we can see, the haze is eliminated clearly and many other objects can not be overwritten.

As for Fig.10, there is another aerial view of the whole image that is almost monotonous in colour. The result image of algorithms [3], [4], [8] show a distorted colour and are clearly demonstrated in Fig.10 (b), Fig.10 (c) and Fig.10 (d). In Fig.10 (e), we can see that the haze image recovered by method [10] often looks blurry and susceptible to gradient reversal effects. Method [11] can dramatically pump up visual effects, while underexposure usually occurred in areas with dark subjects. Fig.10 (h) shows that the DCP method does not apply to the mirror or overexposure areas in the haze images. On the contrary, the improved DCP-based algorithm [16] and our approach can obtain visually compelling dehazing results, as shown in Fig.10 (g) and Fig.10 (i).

A near view scene in dense haze situation is shown in Fig.11(a). The visual performance of seven dehazing techniques and our technique are shown in Fig.11(b)-(i) respectively. The effect of Fig.11(b) has higher contrast than the results of other techniques, while some areas are too bright and have in-homogeneous enhancement. In the results of algorithms [4], [8], [11], the details of haze image can be displayed, however, the colour of image is significantly distorted, especially in the sky region and the edge of the object. The dehazing results of method [10] usually look very fuzzy and are mostly affected by halo problem, as can be seen in Fig.11(e). We note that the result image from Fig.11 (g) is blurred by the edge details, which means that the estimation of the atmospheric light A is inaccurate. As for the effect of the technique [18], there are both halo effect and image noise in sky area, as shown in Fig.11 (h). Since we use the method of modified least-square filter in transmittance, the improved method does not sacrifice the fidelity of colour and expand the halo effect when dealing with the sky area. It can be confirmed in Fig.11(i) that our method can obtain better results in both the close and distant regions.

In short, the improved algorithm can be applied to non-homogeneous haze and dense haze conditions. The atmospheric scattering model and DCP utilized in our technique can obtain the estimation of atmospheric light A and transmittance more accurately. Besides, a small amount of haze preserved in moderation makes the dehazing recovery results more natural as shown in above figures.

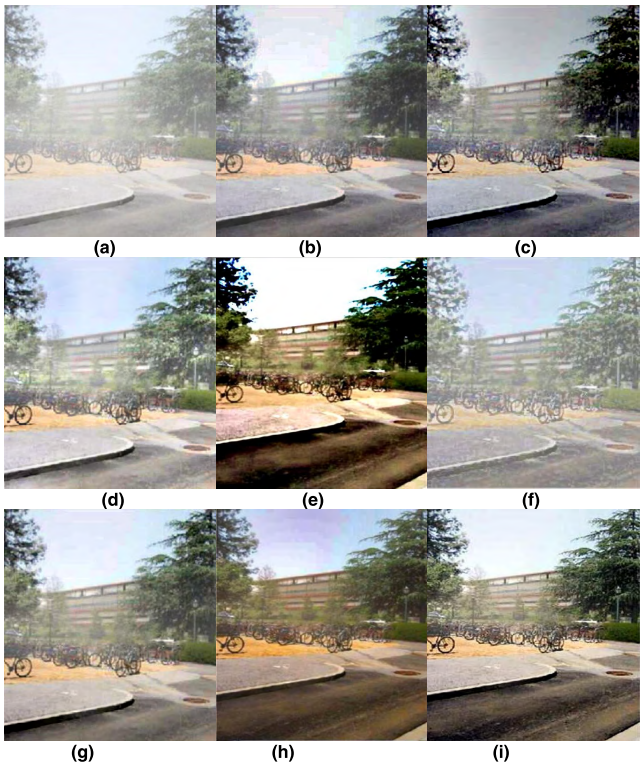

FIGURE 11. Comparison of different dehazing algorithms. (a) Haze image (b) The algorithm [3]. (c) The algorithm [4]. (d) The algorithm [8]. (e) The algorithm [10]. (f) The algorithm [11]. (g) The algorithm [16]. (h) The algorithm [18]. (i) Improved algorithm.

B. COMPARISON OF TIME EFFICIENCY

In order to verify the superiority of our approach in terms of running time, various images of different sizes were used for observation. Comparing our method with the algorithms [3], [4], [8], [10], [11], [16], [18], it can be seen that the approach [18] in table 2 has the poorest process efficiency due to the application of soft matting algorithm to the sparse matrices, which brings about the problem of low computing efficiency. The DCP-based algorithm [16] performs poorly as far as time consumption is concerned. This is due to the use of a distributed ordering method with scaled brightness to select pixel values at the chosen spot of the pictures. Besides, the polarization imaging method will limit the execution performance of the algorithm [8]. The algorithm [3] introduces ICA technique, so as the image size increases the algorithm can maintain high-speed data processing efficiency, even faster than our method. The efficiency of algorithm [4], based on the improved Retinex colour vision model, is also remain fast. Algorithm [10] also has good performance too because it employs the fast Fourier transform in the frequency domain for convolution operation. The approach [11] is advanced by utilizing fast bilateral filter algorithm. However, the processing time will increase when the picture resolution is increased.

TABLE 2. Comparison of time complexity (Unit:ms).

Resolution	280*320	350*550	400*600	500*800	960*1280
Method [3]	263.1	463.03	698.5	885.1	2064.6
Method [4]	305.3	589.4	881.6	1108.3	2671.2
Method [8]	1935.7	5742.9	7355.3	13983.7	21354.2
Method [10]	592.7	1039.4	1568.1	1986.8	2838.7
Method [11]	651.2	3151.5	8297.2	10581.5	15262.6
Method [16]	2293.6	7031.8	9835.2	14351.9	22051.3
Method [18]	5805	10062	15102	18625	26058
Improved method	322.2	564.9	852.2	1079.8	2542.8

C. QUALITY EVALUATION

Since the subjective evaluation has inevitable bias, quality evaluation criteria are usually employed to assess the effects of dehazing results. For a comprehensive evaluation, we not only adopt three full reference evaluation metrics to measure the effectiveness of the algorithms [3], [4], [8], [10], [11], [16], [18], including index MSE [30] (Mean squared error), PSNR [31], [32] (peak signal to noise ratio) and SSIM [28], [32] (Structural similarity), but also add no reference indexes, including e, r, σ.

The MSE [30] can be expressed as Eq.(20).

$$MSE(F', R) = \frac{1}{3IJ}\sum_{x=1'}^{I}\sum_{y=1}^{J}\sum_{c=1}^{3}(F'(x, y, c) - R(x, y, c))^2 \tag{20}$$

where IJ indicates that the image block dimension contains $I \times J$ pixels, subscript c the number of colour channels, F' (x, y, c) the haze removal image, and R (x ,y, c) the haze-free image.

$$PSNR = 10\lg\frac{f_{\max}^2}{MSE} \tag{21}$$

In Eq.(21), $f_{\max}$ denotes the maximum grayscale intensity value. SSIM [28], [32] is the one of the frequently-used ways to measure image quality, and SSIM [28], [32] can be expressed as:

$$SSIM = \frac{1}{IJ}\sum_{x=1'}^{I}\sum_{y=1}^{J}\frac{(2u_{F',x,y}u_{R,x,y} + d_1)(2\alpha_{F'R,x,y} + d_2)}{(u_{F',x,y}^2 + u_{R,x,y}^2 + d_1)(2\alpha_{R,x,y}^2 + \alpha_{F',x,y}^2)} \tag{22}$$

In this paper, we choose an image block of size 3×3, which centered in a pixel point (x, y) of haze removal image F'. $u_{F',x,y}$ and $\alpha_{F',x,y}^2$ represent local mean and variance of the haze removal image, respectively, and $u_{R,xy}$ and $\alpha_{R,xy}^2$ the counterparts of the haze-free image R. $\alpha_{F'R,xy}$ means the covariance between the haze removal and haze-free images in the same scene, which can be estimated by Eq.(23).

$$\alpha_{F'R,x,y} = \frac{1}{xy-1}\sum_{x=1}^{xy}(I_{x,y} - u_{F',x,y})(I_{x,y} - u_{R,x,y}) \tag{23}$$

Here, xy denotes the amount of pixels in the block area, and d_1 and d_2 are usually set as 0.01 and 0.03 according to

the empirical values. After that, we can calculate the average SSIM [28], [32] value of three RGB colour channels.

For our method, the minimum MSE and maximum PSNR values for a single dehazing image are 6.5238 and 24.8659 respectively. Table 3 shows MSE, SSIM_{ave} and PSNR results of the eight different methods. To simplify the calculation, the ratios of MSE and PSNR in parentheses are obtained by dividing 6.5238 and 24.8659 individually.

TABLE 3. Objective comparison of our method and methods [3], [4], [8], [10], [11], [16], [18] using MSE, SSIM_{ave} and PSNR results.

	MSE	SSIM_{ave}	PSNR
Method [3]	10.6583(1.6338)	0.7502	16.9958(0.6835)
Method [4]	10.3189(1.5817)	0.8113	17.7368(0.7133)
Method [8]	9.8831(1.5149)	0.8589	20.6760(0.8315)
Method [10]	12.6721(1.9424)	0.7548	20.4248(0.8214)
Method [11]	11.3325(1.7371)	0.7730	18.7439(0.7538)
Method [16]	8.5807(1.3153)	0.7726	22.7821(0.9162)
Method [18]	9.1526(1.4030)	0.7721	19.5844(0.7876)
Improved method	8.7132(1.3356)	0.8547	22.9537(0.9231)

For the above three metrics, a higher PSNR [31], [32], a larger SSIM [28], [32] or a small value of MSE [30] lead to better results.

For the need of accurate comparison, we should normalize the dimensional distinction of three index types. The equation is represented as follows:

$$b = \frac{(b_{\max} - b_{\min}) \times (a - a_{\min})}{a_{\max} - a_{\min}} + b_{\min} \tag{24}$$

In it, a means the index data, $a_{\max}$ and $a_{\min}$ the highest and lowest values of index data before normalization, $b_{\max}$ and $b_{\min}$ the highest and lowest values of index data after normalization. To simplify the calculation procedure, we set $b_{\max} = 1$ and $b_{\min} = 0.5$.

Since MSE [30] is inversely changed with the other two indexes, the comprehensive evaluation index is given by Eq.(25).

$$Inte = PSNR + SSIM - MSE \tag{25}$$

Table 3 can be converted to a normalization form according to Eq.(25), as shown in Table 4.

TABLE 4. Objective comparison of our method and methods [3], [4], [8], [10], [11], [16], [18] using MSE [30], SSIM_{ave} [28], [32] and PSNR [31], [32] in normalization form.

Index	MSE	SSIM_{ave}	PSNR	*Inte*
Method [3]	0.7539	0.5000	0.5000	0.2461
Method [4]	0.7124	0.7810	0.5621	0.6307
Method [8]	0.6592	1.0000	0.8089	1.1497
Method[10]	1.0000	0.5212	0.7878	0.3927
Method[11]	0.8363	0.6049	0.6467	0.3316
Method[16]	0.5000	0.6030	0.9855	1.4151
Method[18]	0.5699	0.6007	0.7172	0.7480
Improved method	0.5162	0.9807	1.0000	1.4645

The columns in blue, red, green and purple represent the indexes of MSE [30], SSIM_{ave}, PSNR [31], [32] and *Inte,* respectively, and the histogram indicators are utilized in Fig.12 to describe the objective comparison of our method and methods [3], [4], [8], [10], [11], [16], [18]. Among those metrics, MSE represents the average difference between the haze removal image and the haze-free image. SSIM indicates the scene-awareness of the human visual system(HVS), and implies the ability to preserve the structure information of the methods. Besides, a higher result of PSNR indicates that the distortion of the haze removal result is smaller.

As can be seen from Table 3 and Table 4, method [8] provides the best SSIM result. It is because that the visual impact is improved by artificially increasing the contrast and brightness of images. Whereas the MSE and PSNR results of method [8] are not very satisfactory. Method [16] obtains good results of MSE and PSNR while poor result of SSIM due to the inaccurate estimation of A. The algorithm [3] always brings about serious color shift phenomenon and halo effects, so the overall results are poor. The overexposure and image noises lead to poor results of MSE and SSIM in method [10], and too much unwanted information brings about unsatisfactory PSNR result in method [11]. As can be seen from Fig.12, our approach achieves better results among the eight dehazing algorithms. After testing, through our method, you can get the colour fidelity and good dehazing effect of the image structure.

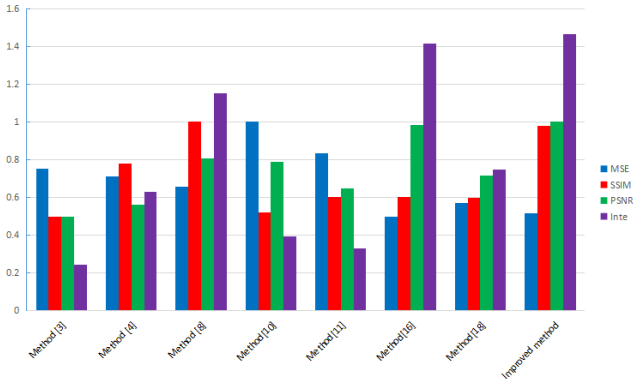

FIGURE 12. Histogram indicators of method [3], [4], [8], [10], [11], [16], [18] and our method.

For no reference image quality assessment, the e indicates the ratio of visible edge recovered from the output of the haze removal results, m_i and m_o the number of visible edges in input and output images.

$$e = \frac{m_o - m_i}{m_i} \tag{26}$$

In Eq.(27), r means the contrast restoration quality in the output image, h_{i} the correlation factor within the set φ, r_{i} the gradients ratio between the input and output image.

$$r = \exp[\frac{1}{m_o} \sum_{h_i \in \varphi} \log(r_i)] \tag{27}$$

Besides, the σ index represents the ratio of over-exposed or under-exposed pixels in output image, m_t the number of

TABLE 5. Objective comparison of our method and methods [3], [4], [8], [10], [11], [16], [18] using e, r and σ.

Index	images	e	r	σ
Method [3]	Fig.7(b)	0.2354	1.6533	0.2587
	Fig.8(b)	0.7018	1.5865	0.2081
	Fig.9(b)	0.1857	1.5368	0.1845
	Fig.10(b)	0.4975	1.7154	0.1312
	Fig.11(b)	0.6057	1.5476	0.1945
Method [4]	Fig.7(c)	0.3102	1.7215	0.2062
	Fig.8(c)	0.5233	1.3292	0.1456
	Fig.9(c)	0.4916	1.6782	0.1227
	Fig.10(c)	0.6059	1.7537	0.1205
	Fig.11(c)	0.6113	1.5095	0.2082
Method [8]	Fig.7(d)	0.5238	**1.7891**	0.1548
	Fig.8(d)	0.6192	1.6084	0.1507
	Fig.9(d)	0.4235	1.7138	0.1539
	Fig.10(d)	0.8019	**1.7662**	0.1275
	Fig.11(d)	0.5941	1.7103	0.1595
Method[10]	Fig.7(e)	0.4915	1.5625	0.2276
	Fig.8(e)	0.1938	1.3117	0.2387
	Fig.9(e)	0.5296	1.4903	0.2597
	Fig.10(e)	0.2133	1.3099	0.2368
	Fig.11(e)	0.7948	1.6938	0.2042
Method[11]	Fig.7(f)	0.3093	1.2314	0.1614
	Fig.8(f)	0.6248	1.3852	0.1678
	Fig.9(f)	0.5173	1.2215	0.1693
	Fig.10(f)	0.7369	1.2160	0.1385
	Fig.11(f)	0.5983	1.2587	0.1412
Method[16]	Fig.7(g)	0.3687	1.2975	0.1175
	Fig.8(g)	0.4072	1.1829	0.1254
	Fig.9(g)	0.6169	1.3973	0.1288
	Fig.10(g)	0.3842	1.3788	0.1223
	Fig.11(g)	0.5614	1.3762	0.1238
Method[18]	Fig.7(h)	0.2228	1.1302	0.1382
	Fig.8(h)	0.3658	1.1535	0.1295
	Fig.9(h)	0.5954	1.3542	0.1479
	Fig.10(h)	0.2615	1.2653	0.1406
	Fig.11(h)	0.4925	1.2804	0.1376
Improved method	Fig.7(i)	**0.5841**	1.7511	**0.0631**
	Fig.8(i)	**0.7319**	**1.6995**	**0.0973**
	Fig.9(i)	**0.8025**	**1.7268**	**0.0802**
	Fig.10(i)	**0.8036**	1.7581	**0.0905**
	Fig.11(i)	**0.8598**	**1.7332**	**0.0649**

pixels beyond the feasible range, and si_x and si_y the size of output image.

$$\sigma = \frac{m_t}{si_x \times si_y} \tag{28}$$

In general, if e and r are bigger, it shows better smog removal, with more levels, abundant details, sharp edges and strong contrast. Whereas a smaller σ implies a better dehazing performance.

As can be seen from Table 5 that our method performs better than methods [3], [4], [8], [10], [11], [16], [18] for e and σ. Fig.7 and Fig.10 demonstrate that the r metric of our method is slightly inferior to method [8], because algorithm [8] increases the contrast of the foggy image to achieve a better result, and hence causes colour shift phenomenon.

V. RESULT AND PROSPECT

The occurrence of haze greatly reduces image and visual quality. Besides, dehazing is a real challenge owing to its ill conditioning nature. Hence, it is essential to research dehazing technologies. In the widely used atmospheric scattering model, the accuracy of atmospheric light and transmittance valuation are the key to effective haze removal.

Based on the innovative approaches of estimation of unknown parameters in atmospheric scattering model, an efficient and effective single image dehazing method is proposed in this paper. In order to obtain a precise value of A and increase accuracy of estimation of transmittance, we use Gray-level threshold segmentation to determine the sky region, then use skyline algorithm to search in the sky area, and replace the guide filter of traditional haze removal method with modified least-square filter algorithm on transmittance. In comparison with approaches [3], [4], [8], [10], [11], [16], [18], although there exist a small amount of image noise and colour shift phenomenon in our dehazing images, the experimental results demonstrate that the image results processed by our method is more vivid, distinct and efficient.

The main contributions of this paper are outlined below.

1) A simple and effective way for processing haze images, especially with large proportion of sky areas, is proposed based on the theory of essence of haze image degradation. Our method demonstrates a good performance in avoiding color shift phenomenon, halo effects and block effects.
2) Two different algorithms are combined to locate and identify the atmospheric light. Our method can overcome the deficiency of low precision of the atmospheric light value and gradient inversion effects in traditional methods.
3) To overcome the ill conditioning problem of atmospheric scattering model, an modified least-square filter is adopted to refine course transmittance. In comparison with previous restoration-based dehazing methods, our method has both impressive and compelling impact on transmittance estimation and the capability of anti-noise.

For our future work, we plan to apply our still image haze removal approach to dynamic video processing.

ACKNOWLEDGEMENT

The authors wish to thank Prof. Lamei Xiao and Prof. Tingting Xiong for fruitful discussions and instruction, Shanika Amarakoon for written language polishing, and the anonymous reviewers for their valuable suggestions.

REFERENCES

[1] T. K. Kim, J. K. Paik, and B. S. Kang, "Contrast enhancement system using spatially adaptive histogram equalization with temporal filtering," *IEEE Trans. Consum. Electron.*, vol. 44, no. 1, pp. 82–87, Feb. 1998.
[2] A. F. M. Raffei, H. Asmuni, R. Hassan, and R. M. Othman, "A low lighting or contrast ratio visible iris recognition using iso-contrast limited adaptive histogram equalization," *Knowl.-Based Syst.*, vol. 74, no. 1, pp. 40–48, Jan. 2015.
[3] B. Jiang, G. A. Woodell, and D. J. Jobson, "Novel multi-scale retinex with color restoration on graphics processing unit," *J. Real-Time Image Process.*, vol. 10, no. 2, pp. 239–253, Jun. 2015.
[4] A. Galdran, A. Alvarez-Gila, A. Bria, J. Vazquez-Corra, and M. Bertalmío, "On the duality between retinex and image dehazing," in *Proc. IEEE Comput. Vis. Pattern Recognit.*, Salt Lake City, UT, USA, Apr. 2018, pp. 1–10.

[5] M.-J. Seow and V. K. Asari, "Ratio rule and homomorphic filter for enhancement of digital colour image," *Neurocomputing*, vol. 69, nos. 7–9, pp. 954–958, Mar. 2006.
[6] S. Dippel, M. Stahl, R. Wiemker, and T. Blaffert, "Multiscale contrast enhancement for radiographies: Laplacian pyramid versus fast wavelet transform," *IEEE Trans. Med. Imag.*, vol. 21, no. 4, pp. 343–353, Apr. 2002.
[7] R. T. Tan, "Visibility in bad weather from a single image," in *Proc. IEEE Conf. Comput. Vis. Pattern Recognit.*, Anchorage, AK, USA, Jun. 2008, pp. 1–8.
[8] W. Zhang, J. Liang, L. Ren, H. Ju, Z. Bai, and Z. Wu, "Fast polarimetric dehazing method for visibility enhancement in HSI colour space," *J. Opt.*, vol. 19, no. 9, p. 095606, Jul. 2017.
[9] R. Fattal, "Single image dehazing," *ACM Trans. Graph.*, vol. 27, no. 3, pp. 988–992, Aug. 2008.
[10] L. Mutimbu and A. Robles-Kelly, "A relaxed factorial Markov random field for colour and depth estimation from a single foggy image," in *Proc. IEEE Int. Conf. Image Process.*, Melbourne, VIC, Australia, Sep. 2013, pp. 355–359.
[11] D. Berman, T. Treibitz, and S. Avidan, "Non-local image dehazing," in *Proc. IEEE Conf. Comput. Vis. Pattern Recognit.*, Las Vegas, NV, USA, Jun. 2016, pp. 1674–1682.
[12] J.-P. Tarel and N. Hautiere, "Fast visibility restoration from a single color or gray level image," in *Proc. IEEE Int. Conf. Comput. Vis.*, Kyoto, Japan, Sep. 2009, pp. 2201–2208.
[13] K. He, J. Sun, and X. Tang, "Single image haze removal using dark channel prior," in *Proc. IEEE Conf. Comput. Vis. Pattern Recognit.*, Miami, FL, USA, Jun. 2009, pp. 1956–1963.
[14] J. Liang, L. Ren, H. Ju, W. Zhang, and E. Qu, "Polarimetric dehazing method for dense haze removal based on distribution analysis of angle of polarization," *Opt. Express*, vol. 23, no. 20, pp. 26146–26157, Oct. 2015.
[15] S. Fang, X. Xia, H. Xing, and C. Chen, "Image dehazing using polarization effects of objects and airlight," *Opt. Express*, vol. 22, no. 16, pp. 19523–19537, Aug. 2014.
[16] Y. Park and T.-H. Kim, "Fast execution schemes for dark-channel-prior-based outdoor video dehazing," *IEEE Access*, vol. 6, pp. 10003–10014, Mar. 2018.
[17] K. He, J. Sun, and X. Tang, "Single image haze removal using dark channel prior," *IEEE Trans. Pattern Anal. Mach. Intell.*, vol. 33, no. 12, pp. 2341–2353, Dec. 2011.
[18] K. He, J. Sun, and X. Tang, "Guided image filtering," *IEEE Trans. Pattern Anal. Mach. Intell.*, vol. 35, no. 6, pp. 1397–1409, Jun. 2013.
[19] L. Liu, N. Yang, J. Lan, and J. Li, "Image segmentation based on gray stretch and threshold algorithm," *Optik Int. J. Light Electron Opt.*, vol. 126, no. 6, pp. 626–629, Mar. 2015.
[20] S. G. Narasimhan and S. K. Nayar, "Interactive (de) weathering of an image using physical models," in *Proc. IEEE Workshop Color Photometric Methods Comput. Vis.*, Paris, France, Oct. 2003, pp. 1–8.
[21] Y. Y. Schechner, S. G. Narasimhan, and S. K. Nayar, "Polarization-based vision through haze," *Appl. Opt.*, vol. 42, no. 3, pp. 511–525, Jan. 2003.
[22] A. Tzanakas, E. Tiakas, and Y. Manolopoulos, "Skyline algorithms on streams of multidimensional data," in *Proc. East Eur. Conf. Adv. Databases Inf. Syst.*, Prague, Czech, Aug. 2016, pp. 63–71.
[23] S.-S. Lin, K. M. Yemelyanov, E. N. Pugh, and N. Engheta, "Separation and contrast enhancement of overlapping cast shadow components using polarization," *Opt. Express*, vol. 14, no. 16, pp. 7099–7108, Aug. 2006.
[24] D. Mortari, "Least-squares solution of linear differential equations," *Mathematics*, vol. 5, p. 48, Feb. 2017.
[25] S. C. Cain and T. Watts, "Nonparaxial Fourier propagation tool for aberration analysis and point spread function calculation," *Opt. Eng.*, vol. 55, no. 8, p. 085104, Aug. 2016.
[26] K. N. Le, K. P. Dabke, and G. K. Egan, "Hyperbolic kernel for time-frequency power spectrum," *Opt. Eng.*, vol. 42, no. 8, pp. 2400–2415, Aug. 2003.
[27] B. Dyda, A. Kuznetsov, and M. KwaŚnicki, "Fractional Laplace operator and Meijer G-function," *Construct. Approx.*, vol. 45, no. 3, pp. 427–448, Jun. 2017.
[28] C. Hillar and S. Marzen, "Revisiting perceptual distortion for natural images: Mean discrete structural similarity index," in *Proc. Data Compress. Conf.*, Snowbird, UT, USA, May 2017, pp. 241–249.
[29] A. Morgand and M. Tamaazousti, "Generic and real-time detection of specular reflections in images," in *Proc. Int. Conf. Comput. Vis. Theory Appl.*, Lisbon, Portugal, Oct. 2015, pp. 274–282.
[30] D. Sandić-Stanković, D. Kukolj, and P. Le Callet, "Image quality assessment based on pyramid decomposition and mean squared error," in *Proc. 23rd Telecommun. Forum Telfor*, Belgrade, Serbia, Jan. 2016, pp. 740–743.
[31] R. Roy and S. Laha, "Optimization of stego image retaining secret information using genetic algorithm with 8-connected PSNR," *Procedia Comput. Sci.*, vol. 60, no. 1, pp. 468–477, Dec. 2015.
[32] A. Horé and D. Ziou, "Image quality metrics: PSNR vs. SSIM," in *Proc. Int. Conf. Pattern Recognit.*, Istanbul, Turkey, Oct. 2010, pp. 2366–2369.
[33] H. Fu, B. Wu, Y. Shao, and H. Zhang, "Perception oriented haze image definition restoration by basing on physical optics model," *IEEE Photon. J.*, vol. 10, no. 3, Jun. 2018, Art. no. 3900816.

HUI FU received the B.E. and M.S. degrees from the School of Information Engineering, Southwest University of Science and Technology, Mianyang, China, in 2014 and 2017, respectively, where she is currently pursuing the Ph.D. degree. Her research interest includes image processing, deep learning, and computer vision.

BIN WU received the B.E. degree from Central South University, Changsha, China, in 1985, and the M.S. and Ph.D. degrees from the University of Science and Technology Beijing, Beijing, China, in 1993 and 1999, respectively. He is currently a Professor with the Southwest University of Science and Technology. His research interests include the most economical intelligent control and image processing.

YANHUA SHAO received the M.S. degree in pattern recognition and intelligent system from the Southwest University of Science and Technology, China, in 2010, and the Ph.D. degree in instrument science and technology from Chongqing University. His research interests include machine learning and image processing.

HONGYING ZHANG received the B.E. degree from Northeastern University, Shenyang, China, in 2000, the M.S. degree from the Southwest University of Science and Technology, Mianyang, China, in 2003, and the Ph.D. degree from the University of Electronic Science and Technology, Chengdu, China. In 2006, she was a Visiting Scholar from the University of Burgundy, Dijon, France. She is currently a Professor with the Southwest University of Science and Technology.